Monthly Notices of the ROYAL ASTRONOMICAL SOCIETY

MNRAS **526,** 2665–2672 (2023) https://doi.org/10.1093/mnras/stad2902
Advance Access publication 2023 September 29

Seen and unseen: bursty star formation and its implications for observations of high-redshift galaxies with *JWST*

Guochao Sun [1]★ Claude-André Faucher-Giguère [1] Christopher C. Hayward [2] and Xuejian Shen [3]

[1] *CIERA and Department of Physics and Astronomy, Northwestern University, 1800 Sherman Avenue, Evanston, IL 60201, USA*
[2] *Center for Computational Astrophysics, Flatiron Institute, 162 Fifth Avenue, New York, NY 10010, USA*
[3] *TAPIR, California Institute of Technology, Pasadena, CA 91125, USA*

Accepted 2023 September 19. Received 2023 September 7; in original form 2023 May 4

ABSTRACT

Both observations and simulations have shown strong evidence for highly time-variable star formation in low-mass and/or high-redshift galaxies, which has important observational implications because high-redshift galaxy samples are rest-ultraviolet (rest-UV) selected and therefore particularly sensitive to the recent star formation. Using a suite of cosmological 'zoom-in' simulations at $z > 5$ from the Feedback in Realistic Environments project, we examine the implications of bursty star formation histories for observations of high-redshift galaxies with *JWST*. We characterize how the galaxy observability depends on the star formation history. We also investigate selection effects due to bursty star formation on the physical properties measured, such as the gas fraction, specific star formation rate, and metallicity. We find the observability to be highly time-dependent for galaxies near the survey's limiting flux due to the star formation rate variability: as the star formation rate fluctuates, the same galaxy oscillates in and out of the observable sample. The observable fraction $f_{\rm obs} = 50$ per cent at $z \sim 7$ and $M_\star \sim 10^{8.5}$–10^9 $\rm M_\odot$ for a *JWST*/NIRCam survey reaching a limiting magnitude of $m_{\rm AB}^{\rm lim} \sim 29$–$30$, representative of surveys such as JADES and CEERS. *JWST*-detectable galaxies near the survey limit tend to have properties characteristic of galaxies in the bursty phase: on average, they show approximately 2.5 times higher cold, dense gas fractions and 20 times higher specific star formation rates at a given stellar mass than galaxies below the rest-UV detection threshold. Our study represents a first step in quantifying selection effects and the associated biases due to bursty star formation in studying high-redshift galaxy properties.

Key words: galaxies: evolution – galaxies: formation – galaxies: high-redshift – galaxies: star formation.

1 INTRODUCTION

The picture of when and how the Universe formed its first generation of galaxies has been revolutionized since the first data release from the *JWST*, even only at the dawn of the *JWST* era. Not only has it enabled unprecedented measurements of the physical properties of the high-redshift galaxy population, such as their mass, star formation rate (SFR), number density, morphology, and chemical evolution (Ferreira et al. 2022; Finkelstein et al. 2022; Naidu et al. 2022; Curtis-Lake et al. 2023; Donnan et al. 2023; Harikane et al. 2023; Labbe et al. 2023; Robertson et al. 2023b; Shapley et al. 2023), the race is on to answer the many intriguing questions posed by the early results (Boylan-Kolchin 2023; Ferrara, Pallottini & Dayal 2023; Kohandel et al. 2023; Mason, Trenti & Treu 2023; Mirocha & Furlanetto 2023).

The search for and identification of high-z galaxy candidates by *JWST* rely primarily on the rest-ultraviolet (rest-UV), multiband photometry in search of the Lyman break. This so-called photometric 'drop-out' technique (Steidel et al. 1996) has proven to be extremely powerful in the hunt of the most distant galaxies over the last three decades using both ground-based and space telescopes. Several major *JWST* observing programmes using this technique are now underway to push the observational frontier of high-z galaxies to newer limits, such as CEERS (Finkelstein et al. 2023), COSMOS-Web (Casey et al. 2023), GLASS-*JWST* (Treu et al. 2022), JADES (Williams et al. 2018; Robertson et al. 2023a), and UNCOVER (Bezanson et al. 2022). Given that the galaxy spectral energy distribution (SED) in the rest-UV is highly sensitive to the recent star formation history (SFH), a good understanding of the SFH is essential to not only the success of the 'drop-out' technique (Furlanetto & Mirocha 2023) but also the inference of physical information that follows (Endsley et al. 2023a; Tacchella et al. 2023).

While most of the SED fitting codes on the market include simple parametrization of time-variable SFHs, both observations and simulations suggest that star formation in high-z galaxies may have occurred in a highly bursty manner (Domínguez et al. 2015; Muratov et al. 2015; Guo et al. 2016; Caputi et al. 2017; Sparre et al. 2017; Faucher-Giguère 2018; Faisst et al. 2019; Rinaldi et al. 2022; Dressler et al. 2023a, b; Endsley et al. 2023b; Looser et al. 2023b) not well described by simple parametrized models, likely due to the strong effects of stellar feedback (Stern et al. 2021; Furlanetto & Mirocha 2022; Hopkins et al. 2023). The burstiness (or duty cycle) of star formation is therefore an important factor to consider in the interpretation of the observed galaxy samples at high redshifts.

In this paper, using simulations from the Feedback in Realistic Environments (FIRE) project,[1] we seek to answer the following

★ E-mail: guochao.sun@northwestern.edu

[1] See the FIRE project website: http://fire.northwestern.edu.

questions about bursty star formation and its implications for high-z galaxy observations with *JWST*: How does the SFR variability impact the galaxy observability by *JWST*? Are there any selection effects on inferred galaxy properties caused by bursty star formation? Answers to these questions not only provide key insights to the interpretation of existing and forthcoming *JWST* observations, but also motivate further studies on the role of bursty star formation in early galaxy formation. In Sun et al. (2023a), for example, we show that these are the same simulations that match the UV luminosity functions (UVLFs) measured by *JWST* at $8 \lesssim z \lesssim 12$, of which the bright end is substantially affected by bursty star formation. Throughout this work, we adopt a flat Lambda cold dark matter cosmology consistent with Planck Collaboration XIII (2016). All magnitudes are quoted in the AB system (Oke & Gunn 1983).

2 METHODS

2.1 The simulations

We analyse the *High-Redshift* suite of the FIRE-2 cosmological zoom-in simulations that were first presented in Ma et al. (2018a, b). These simulations were generated with an identical version of GIZMO (Hopkins 2015) in the meshless finite-mass mode for hydrodynamics. Physical models of the multiphase interstellar medium (ISM), star formation, and stellar feedback used in the FIRE-2 simulations are described in detail by Hopkins et al. (2018). A uniform, redshift-dependent ionizing background is assumed and reionizes the Universe at $z \approx 10$.[2] Several previous studies from the pre-*JWST* era demonstrated that FIRE simulations based on these models reproduced the observed UVLF and galaxy scaling relations, such as stellar mass–halo mass relation, the SFR–stellar mass relation, and the mass–metallicity relation, reasonably well up to $z > 5$ (Ma et al. 2016, 2018b, 2019).

Throughout our analysis, we focus on the well-resolved, central galaxies hosted by main haloes (rather than subhaloes) in the zoom-in region of each simulation. For each central galaxy, we examine 56 consecutive snapshots saved for each simulation, spanning a redshift range of $5 < z < 12$ approximately every 10–20 Myr apart. To analyse the physical properties of galaxies in the 26 simulations considered (Table 1), we first identify the star and gas particles in central galaxies hosted by main haloes, which are found using the spherical overdensity-based AMIGA Halo Finder (AHF; Knollmann & Knebe 2009). AHF locates the haloes in the simulation volume and calculates their basic information such as the centre of mass, virial mass ($M_{\rm vir}$), and virial radius ($R_{\rm vir}$). The evolving virial overdensity definition from Bryan & Norman (1998) is used. The stellar mass ($M_\star$) and gas mass ($M_{\rm gas}$) contents of the galaxy are then defined to be the summed masses of star and gas particles within $0.2R_{\rm vir}$ of the halo centre, respectively. The choice of $0.2R_{\rm vir}$ excludes most satellites and is a simple approximation for properly estimating the stellar and gas properties of central galaxies.

Besides the total stellar and gas masses, we measure and monitor a few other galaxy properties from the simulations to understand their connection with the duty cycle corresponding to the strongly time-variable SFH and implications this might have for *JWST* observations. Using the 'archaeological' approach commonly adopted for studies of the SFR variability (see e.g. Flores Velázquez et al. 2021; Gurvich et al. 2023), we estimate the instantaneous SFR from the distribution of formation times and masses of star particles evaluated at the snapshot corresponding to the redshift of interest. In the low-mass limit most pertinent to our investigation, we expect that the archaeological approach is not significantly affected by *ex situ* star formation contributed by mergers (e.g. Fitts et al. 2018). We have verified this to be a valid approximation for our analysis by comparing the archaeological method with the SFR estimated by evaluating the stellar mass difference between consecutive snapshots. For the gas mass fraction, we define it to be the ratio of the cold and dense gas mass to the sum of stellar and cold and dense gas masses, namely $f_{\rm gas,CD} = M_{\rm gas,CD}/(M_{\rm gas,CD} + M_\star)$. For simplicity, we compute $M_{\rm gas,CD}$ by summing up the masses of gas particles with temperature $T < 300\,{\rm K}$ and density $n > 10\,{\rm cm^{-3}}$. These simple cuts for the gas fraction are adopted because they were found to provide a good proxy for the cold and dense molecular gas available for fuelling star formation in the FIRE simulations (Orr et al. 2018), though we note that more physically motivated descriptions of the molecular gas content could be applied (e.g. Krumholz, McKee & Tumlinson 2008, 2009; McKee & Krumholz 2010). More accurate treatments of ISM chemistry in the cosmic dawn regime should be explored for detailed comparison with observations. We also consider a basic measure of the metallicity of simulated galaxies by keeping track of

Table 1. Properties of the most massive (or the 'primary') galaxy in each of the 26 simulations analysed in this work, including the virial mass, stellar mass, cold and dense gas fraction, specific SFR (sSFR), and gas-phase metallicity, evaluated at $z = 6$ (for `z5mxx`), 8 (for `z7mxx`), and 10 (for `z9mxx`).

Simulation	$M_{\rm vir}$ ($\rm M_\odot$)	$M_\star$ ($\rm M_\odot$)	$f_{\rm gas,CD}$	sSFR ($\rm yr^{-1}$)	$Z_{\rm gas}$ ($\rm Z_\odot$)
z5m11a	1.6e+10	4.0e+7	3.4e−3	7.4e−10	3.0e−1
z5m11b	2.3e+10	6.7e+7	1.4e−1	1.1e−9	2.9e−2
z5m11c	6.2e+10	3.6e+8	3.5e−1	1.6e−8	1.1e−1
z5m11d	9.5e+10	8.9e+8	2.1e−1	6.0e−9	1.4e−1
z5m11e	1.2e+11	3.4e+8	3.6e−1	9.6e−10	6.3e−2
z5m11f	1.7e+11	6.2e+8	2.8e−1	5.8e−9	1.2e−1
z5m11g	9.1e+10	2.1e+8	6.5e−1	4.4e−9	4.3e−2
z5m11h	7.8e+10	3.8e+8	5.9e−1	9.7e−9	6.2e−2
z5m11i	2.6e+10	7.2e+7	0.0e+0	1.4e−12	2.7e+0
z5m12a	2.3e+11	1.4e+9	2.4e−1	1.1e−8	1.5e−1
z5m12b	4.7e+11	1.0e+10	1.2e−1	9.2e−9	2.4e−1
z5m12c	4.7e+11	2.7e+9	3.2e−1	2.2e−9	1.6e−1
z5m12d	3.3e+11	1.9e+9	3.6e−1	1.3e−8	1.2e−1
z5m12e	3.1e+11	4.3e+9	2.3e−1	1.9e−8	2.0e−1
z7m11a	2.3e+11	1.8e+9	4.3e−1	3.7e−8	1.0e−1
z7m11b	5.2e+10	5.5e+7	7.3e−1	1.6e−8	3.3e−2
z7m11c	1.1e+11	8.0e+8	4.5e−1	2.0e−8	7.2e−2
z7m12a	2.9e+11	2.6e+9	2.3e−1	8.6e−9	1.6e−1
z7m12b	3.3e+11	5.8e+9	1.5e−1	9.5e−9	1.9e−1
z7m12c	2.7e+11	1.9e+9	3.0e−1	8.2e−9	1.2e−1
z9m11a	9.1e+10	2.9e+8	4.8e−1	2.0e−8	6.7e−2
z9m11b	1.2e+11	1.3e+9	2.2e−2	4.7e−9	3.2e−1
z9m11c	1.1e+11	1.3e+9	1.5e−1	1.8e−8	2.0e−1
z9m11d	6.8e+10	2.9e+8	1.5e−3	6.9e−10	3.8e−1
z9m11e	7.8e+10	3.6e+8	2.3e−1	1.5e−8	8.1e−2
z9m12a	3.1e+11	6.6e+9	1.8e−1	1.3e−8	1.8e−1

Note. Values of $f_{\rm gas,CD}$, sSFR, and $Z_{\rm gas}$ can vary strongly in time as the SFR fluctuates.

[2]The version of the ionizing background that reionizes the Universe at $z \approx 10$ is a slight update of the original Faucher-Giguère et al. (2009) model from December 2011 (see http://galaxies.northwestern.edu/uvb-fg09).

the overall gas-phase metallicity $Z_{\rm gas} = M_Z/M_{\rm gas}$, based on the mass fraction of *all metals* for the gas particles.

2.2 Processing and analysis

2.2.1 Stellar and nebular emission

To assess the observability of our simulated galaxies by *JWST* surveys, we need to generate mock observations of them and compare with the survey depths. We use a modelling approach similar to Ma et al. (2018a, b) where synthetic, single stellar population spectra are assigned to star particles so as to compute the apparent magnitude and therefore the detectability of each simulated galaxy. Given our interest in comparing against *JWST* surveys of high-z galaxies using the photometric, drop-out technique (Steidel et al. 1996; Robertson 2022), we take into account two additional factors that are neglected in Ma et al. (2018a, b), namely the nebular emission and attenuation by the neutral IGM. The IGM attenuation causes the Lyman break feature, which is the basis of the drop-out technique. The intrinsic emission spectra of galaxies are further reddened by a simple empirical prescription for dust attenuation.

Specifically, we interpolate spectra of binary stars from BPASS v2.2 (Stanway & Eldridge 2018) to model the rest-frame UV/optical emission spectrum of galaxies with realistic SFHs extracted from our high-z simulations, which would be observed at near-infrared wavelengths by *JWST*. We adopt the default stellar initial mass function (IMF), which is described by a broken power law across $0.1\,{\rm M}_\odot < m < 0.5\,{\rm M}_\odot$ and $0.5\,{\rm M}_\odot < m < 300\,{\rm M}_\odot$, with low-mass and high-mass slopes $\alpha_1 = -1.3$ and $\alpha_2 = -2.35$, respectively (Kroupa 2001). It is noteworthy that a non-universal IMF that depends on star-forming environments (e.g. metallicity, interstellar radiation field, gas temperature) could also induce stochasticity in the expected galaxy SED (Chruślińska et al. 2020; Steinhardt et al. 2023). However, we expect the UV variability of galaxies to be primarily driven by the time-variable SFH, given the order-of-magnitude fluctuations in the SFR, and thus postpone the investigation of such IMF effects to further work. For each star particle, we take the combination of the stellar age, $t_{\rm age}$, and metallicity, $Z_\star$, to evaluate the spectral emissivity (per unit mass of stars formed) required to scale the star particle's luminosity by its mass. Namely, the specific luminosity of the galaxy at a cosmic time t can be written as $\sum_i L_\nu^i \left(t_{\rm age}^i, Z_\star^i\right)$, where $t_{\rm age}^i = t - {\rm SFT}_i$ is the stellar age of star particle i defined as the difference between the cosmic time at the rest frame of the observed galaxy and the star formation time of the star particle.

Regarding nebular emission lines, although one might expect these lines to have only secondary effects on the photometry of galaxies compared to the stellar continuum, especially for wide-band filters of *JWST* considered in this work, it is important to include them for better understanding e.g. their impact on the apparent magnitudes relative to effects of the SFR variability and the dependence on assumptions made for stellar populations, such as single versus binary stars. Similar considerations also apply to the nebular continuum emission, whose contribution to the net rest-UV/optical flux can be non-negligible especially at longer wavelengths and for young stellar populations (Byler et al. 2017). To implement the nebular emission (both lines and continuum), we use the BPASS data products from the BPASS v2.2 data release (Stanway & Eldridge 2018; see also Xiao, Stanway & Eldridge 2018 for an early release of nebular line predictions based on BPASS v2.1 models), where SED templates with nebular emission included are generated with CLOUDY (Ferland et al. 2017) and tabulated for grids of $t_{\rm age}$ and $Z_\star$, together with ISM properties including the gas density $n_{\rm H}$ and ionization parameter U. Assuming $n_{\rm H} = 100\,{\rm cm}^{-3}$ and $U = 0.01$, broadly consistent with the ionized gas properties inferred for high-z galaxies from recent *JWST* observations (Reddy et al. 2023), we use the CLOUDY-processed SED templates to derive the flux contribution from each star particle. We stress that these physically motivated but ultimately simplistic prescriptions for the nebular emission are not intended to create high-accuracy mock galaxy spectra, but rather to help gauge the impact of accounting for the nebular emission in general.

2.2.2 IGM attenuation

Due to the opacity of intergalactic neutral hydrogen to UV photons, the spectra of high-z galaxies are filtered by a blanketing effect causing increasing absorption blueward of Ly$\,\alpha$ (1216 Å) till the Lyman-limit wavelength (912 Å), beyond which the absorption becomes complete. Such intergalactic medium (IGM) transmission effects create the Lyman-break feature in the observed galaxy spectrum, and we account for them with an analytical model introduced by Inoue et al. (2014) widely used for the modelling of high-z galaxy spectra recently observed by *JWST*.

2.2.3 Dust attenuation

Overall, based on empirical models for the dependence of dust attenuation on the dust content of galaxies, we expect dust attenuation to be small (i.e. $A_\lambda = 1.086\tau_\lambda \ll 1$) for the low-mass ($M_\star \lesssim 10^{8.5}\,{\rm M}_\odot$) systems at high-$z$, for which we find the largest duty cycle effects of interest to this work (see Section 3). This is further supported by several recent characterizations of dust attenuation at high redshifts based on *JWST* measurements of the Balmer decrement (Shapley et al. 2023) or fits to the observed galaxy UVLFs and colours (Mirocha & Furlanetto 2023). For completeness, though, we include a conservative, empirical description of dust attenuation following McLure et al. (2018). Combining deep imaging data from the Atacama Large Millimeter Array at 1.3 mm and other multiwavelength data available at optical/infrared of the Hubble Ultra Deep Field, McLure et al. (2018) study the relationship among the infrared excess, UV spectral slope, and $M_\star$ for a sizeable sample of star-forming galaxies at $2 < z < 3$ and use it to constrain the amount of dust attenuation as a function of $M_\star$. We adopt their best-fitting relation between A_{1600} and $M_\star$ given by a third-order polynomial in $X = \log(M_\star/10^{10}\,{\rm M}_\odot)$, and use it to determine A_λ as a function of $M_\star$, assuming $\tau_\lambda \propto \lambda^{-1}$ as expected for a Small Magellanic Cloud-like extinction curve (Weingartner & Draine 2001; Ma et al. 2019).

3 RESULTS

Comparing the set of post-processed simulations with *JWST* observations (Section 2), we examine how the time-variable SFH of individual high-z galaxies impacts their detectability by *JWST* and characterize physical properties of the galaxy population revealed or concealed by a given *JWST* photometric survey. For the main results that follow, we consider the comparison with a photometric galaxy survey with depth similar to JADES-Deep (Williams et al. 2018),[3] reaching a limiting magnitude of $m_{\rm AB}^{\rm lim} \sim 30.6$

[3]JADES-Medium/Deep also utilizes two shallower mid-band filters (Fig. 2), but for simplicity we only focus on the wide-band filters.

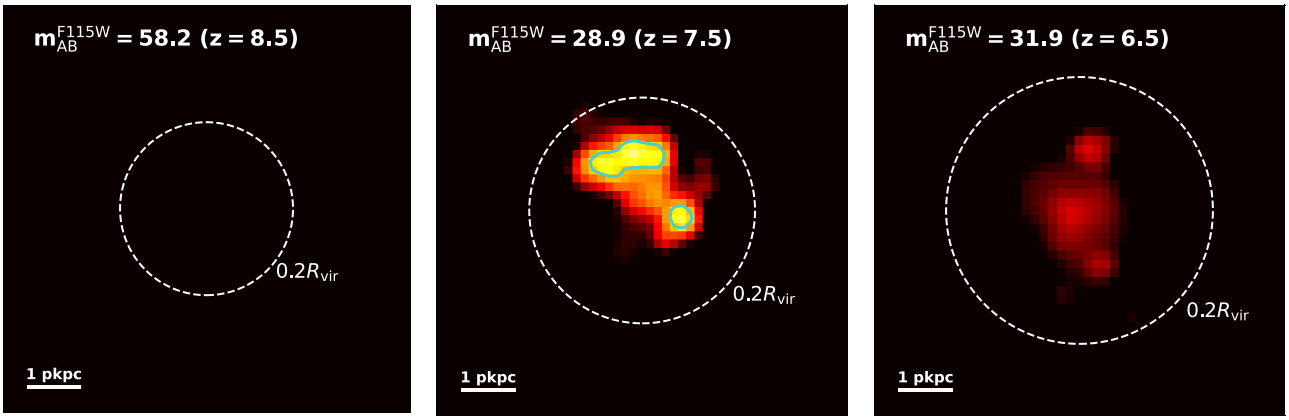

Figure 1. Noiseless, PSF-convolved *JWST*/NIRCam mock images of the example galaxy z5m11d at $z = 8.5$, 7.5, and 6.5 in band $F115W$ with pixel size 0.031 arcsec. The PSF is assumed to be Gaussian, with an FWHM of 2 pixels (Ma et al. 2018b). The contour marks the 1σ surface brightness sensitivity level corresponding to 26.5 mag arcsec^{-2}, which is converted from the point-source limiting magnitude of a JADES-Deep-like survey. The apparent magnitude, m_{AB}^{F115W}, of the galaxy at each redshift is labelled on the top left corner. Note the huge m_{AB}^{F115W} value caused by strong IGM absorption when band $F115W$ probes blueward of the Lyman break at $z \gtrsim 8.5$ and the time variations of the galaxy flux and apparent size as a strong starburst occurs at $z \approx 7.5$ (see the upper panel of Fig. 2), which causes the galaxy to oscillate into (out of) the observable regime from $z = 8.5$ (7.5) to $z = 7.5$ (6.5).

for 5σ point-source detections in the NIRCam wide-band filters. Besides this fiducial survey, we also inspect how these results depend on the survey depth by repeating the same analysis for two additional surveys similar to JADES-Medium and CEERS, which are approximately 1 and 2 mag shallower than JADES-Deep, respectively.

3.1 Effects of SFR variations on the galaxy observability

Due to the fact that the rest-UV selection for high-z galaxies is highly sensitive to the recent SFH, we find a strong coherence between the SFR and apparent magnitude of the galaxies. Such a coherence leads to the migration of a given galaxy into, and out of, the observable regime as the galaxy's SFR varies, which is particularly true for galaxies near the detection threshold of the survey. Fig. 1 shows *JWST*/NIRCam mock images of the primary galaxy of z5m11d in band $F115W$ at $z = 8.5$, 7.5, and 6.5 (from left to right), generated after convolving high-resolution simulated images with a Gaussian point spread function (PSF) corresponding to band $F115W$. From these mock images, two key features of the connection between SFR variations and the observability are apparent: as the SFR of galaxies like z5m11d undergoes strong variations, there are both up and down movements in flux, as shown by the colour coding, and fluctuations of the apparent size (above the surface brightness detection limit) concurrent with flux variations, as indicated by the contours. We emphasize that these mock images are shown only for illustration purpose. For the analysis that follows, we determine the observability of galaxies by comparing the apparent magnitude against the 5σ limiting magnitude of the survey of interest.

In Fig. 2, we illustrate the modulation of the galaxy's detectability by *JWST* due to the strong time variability of the SFR. As highlighted in the top panel, the two example galaxies, z5m11d and z5m12b, experience a major outburst of star formation at $z \sim 7.5$ and $z \sim 10.5$, respectively. The rapid and substantial rise and fall of the SFR associated with the starburst can temporarily brighten these originally too-faint-to-detect galaxies by several magnitudes, making them detectable for a period of time before fading off again as the massive, young stars formed in the starburst die. Throughout,

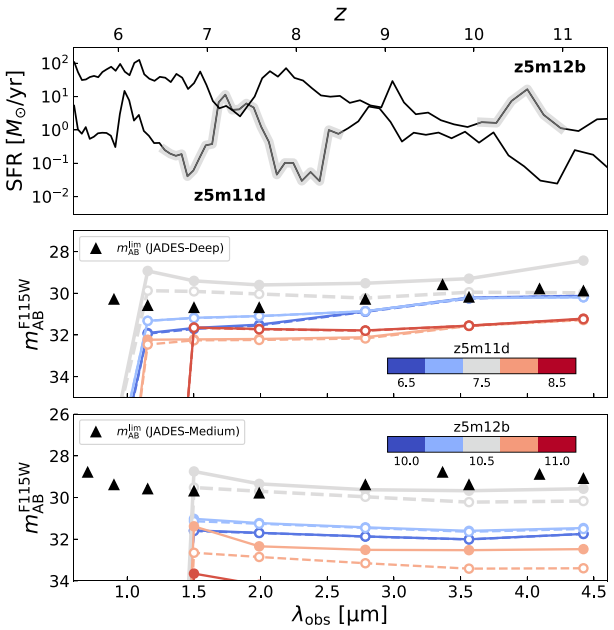

Figure 2. Impact of bursty SFH on the observability of two example galaxies, z5m11d and z5m12b, from our simulations. *Top*: Time variability of the SFR evaluated for an averaging time-scale of 10 Myr. Highlighted segments show the redshift intervals inspected below for the observability. *Middle*: Apparent magnitudes of z5m11d in *JWST*/NIRCam filters ($F070W$, $F090W$, $F115W$, $F150W$, $F200W$, $F277W$, $F356W$, $F444W$), with (filled symbols/solid lines) or without (empty symbols/dashed lines) including the nebular emission. Lines are colour-coded by redshift for five snapshots of the galaxy. The triangles indicate 5σ limiting magnitudes of the JADES-Deep survey (Williams et al. 2018). *Bottom*: Same as the middle panel but for z5m12b and the JADES-Medium survey.

we consider a galaxy to be detectable if and only if there are (1) at least two $>5\sigma$ detections redward of the Lyman break and (2) no detections blueward of it (i.e. the 'drop-out' can be detected at high significance). Also noteworthy from the comparison between cases with and without the nebular emission is that changes in

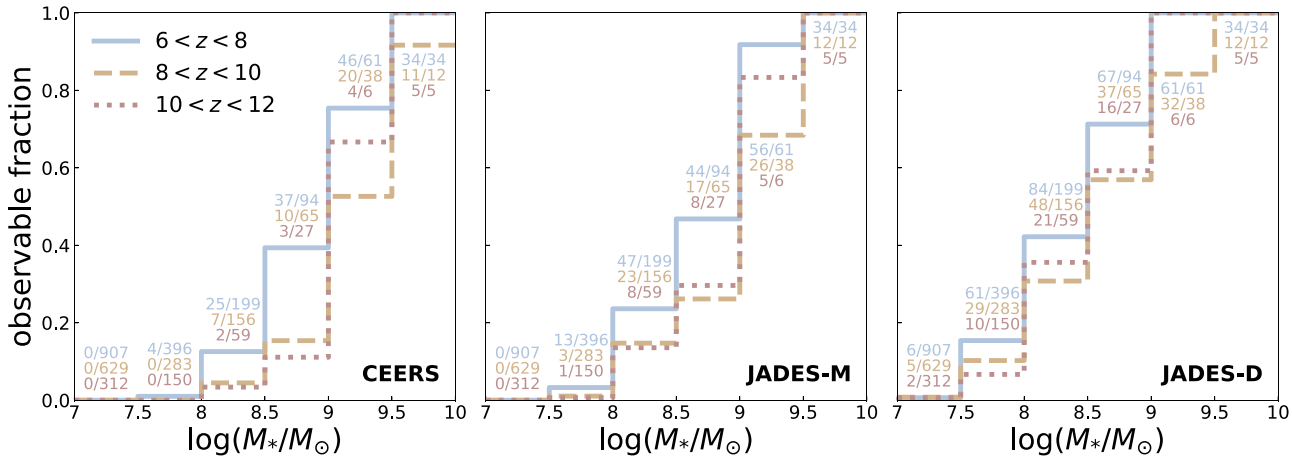

Figure 3. The observable fraction, $f_{\rm obs} = N_{\rm obs}/N_{\rm tot}$, defined as the ratio of detectable and total numbers of galaxies in each bin, of galaxies at $z = 6$–12 for the three example *JWST* survey depths considered (left: CEERS, middle: JADES-Medium, and right: JADES-Deep). Bursty star formation affects the observability the most at mass scales where $f_{\rm obs} \approx 50$ per cent, which increase with decreasing depth or increasing redshift and roughly correspond to $M_\star \sim 10^{8.5}$–10^9 M$_\odot$ for the surveys and redshift ranges displayed.

the observability induced by bursty star formation become more significant when the nebular emission tracing recent star formation is taken into account.

While only two examples are shown in Fig. 2, the non-monotonic evolution of a galaxy's observability imprinted by its bursty SFH is ubiquitous in our simulations, especially in the mass and redshift range where galaxies are marginally detectable/non-detectable. To demonstrate and identify in what mass and redshift ranges galaxies are near the detection threshold and thus subject to a strong influence by bursty star formation, we show in Fig. 3 the observable fraction, $f_{\rm obs}$, together with the raw numbers of snapshots ($N_{\rm obs}/N_{\rm tot}$) used to evaluate $f_{\rm obs}$, of galaxies in different $M_\star$ bins in three redshift ranges and for three example survey depths. Overall, $f_{\rm obs}$ increases towards higher masses in a given redshift range, whereas at a given mass $f_{\rm obs}$ declines with increasing redshift. For the survey depths considered, across the redshift ranges examined, $f_{\rm obs} \sim 50$ per cent for galaxies with $M_\star \sim 10^{8.5}$–10^9 M$_\odot$. This can be viewed as a characteristic mass at which bursty star formation affects observability the most. The $f_{\rm obs} \sim 50$ per cent mass scale increases for a shallower survey (e.g. CEERS) and decreases for a deeper survey (e.g. JADES-Deep), but broadly falls within the range of $10^{8.5} \lesssim M_\star/{\rm M}_\odot \lesssim 10^9$ for the surveys considered. For a given survey, the mass scale increases slightly with redshift. We note that other galaxy properties and their evolution with mass and redshift may also impact their observability.

3.2 Global properties of galaxies seen and unseen by *JWST*

Given the strong oscillations in the observability of a galaxy that are induced by its SFR variability, a natural question is whether such a modulation introduces significant selection effects. To address this question, we perform a simple classification of our simulated galaxies, after combining all the available snapshots to increase the sample size, according to their observability by our fiducial example survey (JADES-Deep). We then examine several global properties of the detectable (D) and non-detectable (ND) galaxies separately, including $f_{\rm gas,CD}$, the specific SFR (sSFR), and $Z_{\rm gas}$. Motivated by the distribution of $f_{\rm obs}$ shown in Fig. 3, we focus on the fiducial survey (JADES-Deep) and consider a narrow mass bin centred around $M_\star = 10^{8.5}$ M$_\odot$ to minimize the influence on our analysis of mass dependence of these properties.

For a narrow mass range of $8.2 < \log(M_\star/{\rm M}_\odot) < 8.8$ where there is a mixture of detectable and non-detectable galaxies at roughly the same $M_\star$, Fig. 4 shows the distributions of the three physical properties of interest estimated from our galaxies classified by their observability. As indicated by both the histograms and Gaussian kernel density estimations (KDEs), different levels of offset between the detectable and non-detectable populations are observed, which we quantify using the median value of either sample in the narrow mass bin considered.

For $f_{\rm gas}$ and sSFR, clear systematic offsets exist, which suggest that detectable galaxies have preferentially more abundant cold and dense gas, as well as higher sSFRs. This is qualitatively in line with our expectations for galaxies having an ongoing burst of star formation – a large mass of cold, dense molecular gas is present as fuel for star formation while many young stars are actively forming. Therefore, it is likely that galaxies being observable thanks to an ongoing starburst can lead to a significant selection bias for higher $f_{\rm gas}$ and sSFR, characteristic of galaxies in the starburst phase. Based on the galaxy samples displayed in Fig. 4, we estimate the systematic difference in the median $f_{\rm gas,CD}$ and sSFR of the detectable and non-detectable populations to be $\Delta f_{\rm gas,CD} \approx 0.4$ dex and ΔsSFR ≈ 1.2 dex. In terms of the offset between median properties of observable galaxies and *all* galaxies in the mass bin considered, we find the fractional differences to be $|f^{\rm obs}_{\rm gas,CD} - f^{\rm all}_{\rm gas,CD}|/f^{\rm all}_{\rm gas,CD} \approx 40$ per cent and $|{\rm sSFR}^{\rm obs} - {\rm sSFR}^{\rm all}|/{\rm sSFR}^{\rm all} \approx 300$ per cent, respectively. These values reflect how representative the observable sample might be for quantifying the relation between median galaxy properties and M_*.

On the other hand, we do not observe an as clear offset for $Z_{\rm gas}$, which arguably relates to the SFR variability less directly. Nevertheless, we note that a lower $Z_{\rm gas}$ for the detectable population (e.g. at $z = 10$–12) could be associated with the plausible scenario where bursty galaxies 'up-scattered' into the observable regime tend to have a higher supply of pristine, star-forming gas that reduces $Z_{\rm gas}$. While such a picture is essentially what the gas-regulator model (Lilly et al. 2013) suggests as a potential explanation for the so-called fundamental metallicity relation, more detailed analysis of

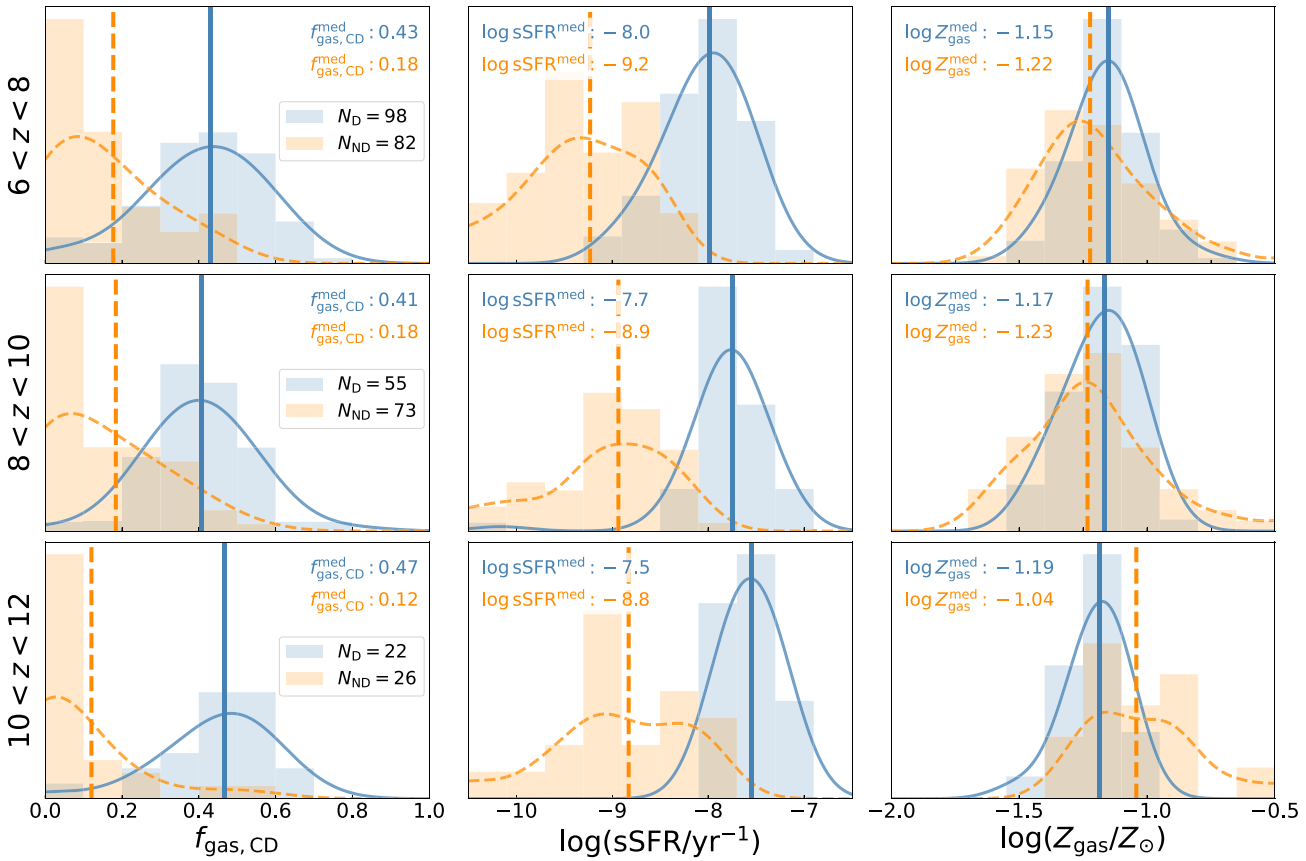

Figure 4. Distributions of physical properties ($f_{\rm gas}$, sSFR, $Z_{\rm gas}$) of galaxies at $6 < z < 8$ (top), $8 < z < 10$ (middle), and $10 < z < 12$ (bottom) detectable ('D', blue) and non-detectable ('ND', orange) by a JADES-Deep-like survey with *JWST*. The narrow stellar mass interval, $8.2 < \log(M_\star/{\rm M}_\odot) < 8.8$, represents a mass regime where there is a mixture of detectable and non-detectable galaxies and therefore close to the detectable threshold of the survey. Median values of each property measured from a Gaussian KDE are specified on the panels for the detectable versus non-detectable samples.

the simulations is required to reach a conclusive answer, which we postpone to future work.

In addition to the distributions shown in Fig. 4 for a narrow mass bin near the detection threshold, we are also interested in quantifying how much the burstiness-induced selection effect could bias the measured galaxy properties as far as a real galaxy population is concerned. To do this, we calculate the average of each galaxy property, weighted by the halo mass function (HMF),[4] ${\rm d}n/{\rm d}M_{\rm vir}$, evaluated at the galaxy's halo mass and redshift, for *all* galaxies with $M_\star > 10^{8.2}\,{\rm M}_\odot$ in the detectable or non-detectable sample for the same redshift ranges shown in Fig. 4. As expected, since lower mass galaxies are more numerous, similar offsets (∼0.4 dex for $f_{\rm gas,CD}$, ∼1.2 dex for sSFR, and insignificant for $Z_{\rm gas}$) are observed between the HMF-weighted average properties of detectable and non-detectable galaxies when considering a narrow mass bin near the detection threshold. Therefore, the offsets in galaxy properties shown in Fig. 4 are broadly representative of biases expected when galaxy properties are averaged over an entire survey.

Finally, by repeating the same analysis for the other two example survey depths (JADES-Medium and CEERS), we find comparable offsets as for the fiducial case of a JADES-Deep-like depth. The main difference is that the sample size of the detectables and the mass range where the bias will have greatest impact ($f_{\rm obs} \sim 50$ per cent) depend on survey depth (see Fig. 3).

[4]We compute the HMF using the HMF code (Murray, Power & Robotham 2013), assuming the fitting function from Behroozi, Wechsler & Conroy (2013) optimized for high redshifts.

4 CONCLUSIONS

In summary, the ubiquitous presence of bursty star formation in low-mass/high-z galaxies predicted by the state-of-the-art simulations of galaxy formation calls for a careful examination of its impact on existing and forthcoming observations. By analysing the *High-Redshift* suite of FIRE-2 simulations for the observability of galaxies with bursty SFHs by *JWST*, we approach this problem in the context of recent *JWST* observing programmes for studying galaxy formation at high redshift. We have reached the following main conclusions:

(i) The strong time variability of the SFR in high-z galaxies introduces a modulation of their brightness (and apparent size) by up to several apparent magnitudes, resulting in non-monotonic time evolution in the observability of galaxies close to the limiting depth of the survey. This effect is enhanced when the nebular emission tracing recent star formation is considered. The time-variable SFRs imply that, at a given $M_\star$, some galaxies will be detectable while others not in rest-UV-selected samples. The stellar mass scale of $f_{\rm obs} \sim 50$ per cent observability depends on survey depth and is $M_\star \sim 10^{8.5}$–$10^9\,{\rm M}_\odot$ at $z \sim 7$ for a *JWST*/NIRCam survey reaching a

limiting magnitude of $m_{\rm AB}^{\rm lim} \approx 29$–$30$, representative of surveys such as JADES and CEERS.

(ii) Systematic offsets in galaxy properties are predicted between galaxy samples detectable and non-detectable by *JWST*. This implies that non-trivial selection effects from bursty SFHs may exist in flux-limited surveys, especially for physical properties closely related to the duty cycle, such as the mass fraction of cold and dense gas and the sSFR. On mass scales where galaxies are marginally detectable/non-detectable, we estimate the selection effect to cause the $f_{\rm gas,CD}$ to be higher by a factor of 2.5 (or 0.4 dex) and the sSFR to be higher by up to order of 20 (or 1.2 dex) for detectable galaxies relative to non-detectable galaxies in the same stellar mass bin. Since low-mass galaxies are the most abundant, the biases predicted for galaxies near the survey limit are representative of biases in galaxy properties averaged over entire surveys.

The observational implications of bursty star formation extend beyond what has been examined in this work. The assumed SFH, if incorrectly neglecting burstiness, can greatly bias stellar masses inferred from SED modelling (e.g. Endsley et al. 2023a). Moreover, as demonstrated in Sun et al. (2023a), bursty SFHs can substantially affect the UV luminosity function especially at the bright end, which in turn impacts analyses based on the widely used halo abundance matching technique (Dekel et al. 2023; Furlanetto & Mirocha 2023; Mason et al. 2023; Muñoz et al. 2023; Shen et al. 2023). Another implication of time-variable SFHs is that low-mass galaxies may appear quiescent between bursts of star formation (Gelli et al. 2023; Looser et al. 2023a). We will explore these aspects, along with effects on other key physical properties such as galaxy size and kinematics, with better statistics in future work. Meanwhile, the impact on observability and selection effects on inferred galaxy properties due to bursty star formation explored here are unlikely to be unique to the study of galaxies at $z > 5$. Observations at lower redshift, such as at cosmic noon ($z \sim 2$–3) where survey selection is also frequently done in the rest-UV (e.g. Steidel et al. 2014), may also be subject to similar effects. It will be interesting for future work to characterize the effects of bursty star formation in other contexts. Finally, our analysis also motivates explorations of ways to probe bursty star formation observationally and characterize its mass and redshift dependence (see e.g. Muñoz et al. 2023; Sun et al. 2023b), which are essential for revealing the origin of stochasticity in the SFH of galaxies.

ACKNOWLEDGEMENTS

The authors thank Jordan Mirocha and Allison Strom for useful discussions. GS was supported by a CIERA Postdoctoral Fellowship. CAFG was supported by NSF through grant AST-2108230 and CAREER award AST-1652522, by NASA through grants 17-ATP17-0067 and 21-ATP21-0036, by STScI through grant HST-GO-16730.016-A, by CXO through grant TM2-23005X, and by the Research Corporation for Science Advancement through a Cottrell Scholar Award. The Flatiron Institute is supported by the Simons Foundation. The simulations used in this paper were run on XSEDE computational resources (allocations TG-AST120025, TG-AST130039, TG-AST140023, and TG-AST140064). Additional analysis was done using the Quest computing cluster at Northwestern University.

DATA AVAILABILITY

The data supporting the plots and analysis in this article are available on reasonable request to the corresponding author. A subset of FIRE-2 simulation snapshots is publicly available at http://flathub.flatironinstitute.org/fire (Wetzel et al. 2023). Additional FIRE data products are available at https://fire.northwestern.edu/data. A public version of the GIZMO code is available at http://www.tapir.caltech.edu/~phopkins/Site/GIZMO.html.

REFERENCES

Behroozi P. S., Wechsler R. H., Conroy C., 2013, ApJ, 770, 57
Bezanson R. et al., 2022, preprint (arXiv:2212.04026)
Boylan-Kolchin M., 2023, Nat. Astron., 7, 731
Bryan G. L., Norman M. L., 1998, ApJ, 495, 80
Byler N., Dalcanton J. J., Conroy C., Johnson B. D., 2017, ApJ, 840, 44
Caputi K. I. et al., 2017, ApJ, 849, 45
Casey C. M. et al., 2023, ApJ, 954, 31
Chruślińska M., Jeřábková T., Nelemans G., Yan Z., 2020, A&A, 636, A10
Curtis-Lake E. et al., 2023, Nat. Astron., 7, 622
Dekel A., Sarkar K. S., Birnboim Y., Mandelker N., Li Z., 2023, MNRAS, 523, 3201
Domínguez A., Siana B., Brooks A. M., Christensen C. R., Bruzual G., Stark D. P., Alavi A., 2015, MNRAS, 451, 839
Donnan C. T. et al., 2023, MNRAS, 518, 6011
Dressler A. et al., 2023a, preprint (arXiv:2306.02469)
Dressler A. et al., 2023b, ApJ, 947, L27
Endsley R., Stark D. P., Whitler L., Topping M. W., Chen Z., Plat A., Chisholm J., Charlot S., 2023a, MNRAS, 524, 2312
Endsley R. et al., 2023b, preprint (arXiv:2306.05295)
Faisst A. L., Capak P. L., Emami N., Tacchella S., Larson K. L., 2019, ApJ, 884, 133
Faucher-Giguère C.-A., 2018, MNRAS, 473, 3717
Faucher-Giguère C.-A., Lidz A., Zaldarriaga M., Hernquist L., 2009, ApJ, 703, 1416
Ferland G. J. et al., 2017, Rev. Mex. Astron. Astrofis., 53, 385
Ferrara A., Pallottini A., Dayal P., 2023, MNRAS, 522, 3986
Ferreira L. et al., 2022, ApJ, 938, L2
Finkelstein S. L. et al., 2022, ApJ, 940, L55
Finkelstein S. L. et al., 2023, ApJ, 946, L13
Fitts A. et al., 2018, MNRAS, 479, 319
Flores Velázquez J. A. et al., 2021, MNRAS, 501, 4812
Furlanetto S. R., Mirocha J., 2022, MNRAS, 511, 3895
Furlanetto S. R., Mirocha J., 2023, MNRAS, 523, 5274
Gelli V., Salvadori S., Ferrara A., Pallottini A., Carniani S., 2023, ApJ, 954, L11
Guo Y. et al., 2016, ApJ, 833, 37
Gurvich A. B. et al., 2023, MNRAS, 519, 2598
Harikane Y. et al., 2023, ApJS, 265, 5
Hopkins P. F., 2015, MNRAS, 450, 53
Hopkins P. F. et al., 2018, MNRAS, 480, 800
Hopkins P. F. et al., 2023, MNRAS, 525, 2241
Inoue A. K., Shimizu I., Iwata I., Tanaka M., 2014, MNRAS, 442, 1805
Knollmann S. R., Knebe A., 2009, ApJS, 182, 608
Kohandel M., Ferrara A., Pallottini A., Vallini L., Sommovigo L., Ziparo F., 2023, MNRAS, 520, L16
Kroupa P., 2001, MNRAS, 322, 231
Krumholz M. R., McKee C. F., Tumlinson J., 2008, ApJ, 689, 865
Krumholz M. R., McKee C. F., Tumlinson J., 2009, ApJ, 693, 216
Labbe I. et al., 2023, Nature, 616, 266
Lilly S. J., Carollo C. M., Pipino A., Renzini A., Peng Y., 2013, ApJ, 772, 119
Looser T. J. et al., 2023a, preprint (arXiv:2302.14155)
Looser T. J. et al., 2023b, preprint (arXiv:2306.02470)
Ma X., Hopkins P. F., Faucher-Giguère C.-A., Zolman N., Muratov A. L., Kereš D., Quataert E., 2016, MNRAS, 456, 2140
Ma X. et al., 2018a, MNRAS, 477, 219
Ma X. et al., 2018b, MNRAS, 478, 1694
Ma X. et al., 2019, MNRAS, 487, 1844
McKee C. F., Krumholz M. R., 2010, ApJ, 709, 308

McLure R. J. et al., 2018, MNRAS, 476, 3991
Mason C. A., Trenti M., Treu T., 2023, MNRAS, 521, 497
Mirocha J., Furlanetto S. R., 2023, MNRAS, 519, 843
Muñoz J. B., Mirocha J., Furlanetto S., Sabti N., 2023, MNRAS, 526, L47
Muratov A. L., Kereš D., Faucher-Giguère C.-A., Hopkins P. F., Quataert E., Murray N., 2015, MNRAS, 454, 2691
Murray S. G., Power C., Robotham A. S. G., 2013, Astron. Comput., 3–4, 23
Naidu R. P. et al., 2022, ApJ, 940, L14
Oke J. B., Gunn J. E., 1983, ApJ, 266, 713
Orr M. E. et al., 2018, MNRAS, 478, 3653
Planck Collaboration XIII, 2016, A&A, 594, A13
Reddy N. A., Topping M. W., Sanders R. L., Shapley A. E., Brammer G., 2023, ApJ, 952, 167
Rinaldi P., Caputi K. I., van Mierlo S. E., Ashby M. L. N., Caminha G. B., Iani E., 2022, ApJ, 930, 128
Robertson B. E., 2022, ARA&A, 60, 121
Robertson B. E. et al., 2023a, Nat. Astron.,7, 611
Robertson B. E. et al., 2023b, ApJ, 942, L42
Shapley A. E., Sanders R. L., Reddy N. A., Topping M. W., Brammer G. B., 2023, ApJ, 954, 157
Shen X., Vogelsberger M., Boylan-Kolchin M., Tacchella S., Kannan R., 2023, MNRAS, 525,3254
Sparre M., Hayward C. C., Feldmann R., Faucher-Giguère C.-A., Muratov A. L., Kereš D., Hopkins P. F., 2017, MNRAS, 466, 88
Stanway E. R., Eldridge J. J., 2018, MNRAS, 479, 75
Steidel C. C., Giavalisco M., Dickinson M., Adelberger K. L., 1996, AJ, 112, 352
Steidel C. C. et al., 2014, ApJ, 795, 165
Steinhardt C. L., Kokorev V., Rusakov V., Garcia E., Sneppen A., 2023, ApJ, 951, L40
Stern J. et al., 2021, ApJ, 911, 88
Sun G., Faucher-Giguère C.-A., Hayward C. C., Shen X., Wetzel A., Cochrane R. K., 2023a, preprint (arXiv:2307.15305)
Sun G., Lidz A., Faisst A. L., Faucher-Giguère C.-A., 2023b, MNRAS, 524, 2395
Tacchella S. et al., 2023, MNRAS, 522, 6236
Treu T. et al., 2022, ApJ, 935, 110
Weingartner J. C., Draine B. T., 2001, ApJ, 548, 296
Wetzel A. et al., 2023, ApJS, 265, 44
Williams C. C. et al., 2018, ApJS, 236, 33
Xiao L., Stanway E. R., Eldridge J. J., 2018, MNRAS, 477, 904

This paper has been typeset from a TEX/LATEX file prepared by the author.